Chemical Science

ROYAL SOCIETY OF CHEMISTRY

EDGE ARTICLE

View Article Online
View Journal | View Issue

Check for updates

Cite this: *Chem. Sci.*, 2022, **13**, 13948

All publication charges for this article have been paid for by the Royal Society of Chemistry

Received 26th October 2022
Accepted 9th November 2022

DOI: 10.1039/d2sc05915k

rsc.li/chemical-science

Open Access Article. Published on 18 November 2022. Downloaded on 2/18/2026 2:20:38 PM.
This article is licensed under a Creative Commons Attribution-NonCommercial 3.0 Unported Licence.

Novel lanthanide nanoparticle frameworks for highly efficient photoluminescence and hypersensitive detection†

Yuan-Jun Tong,[a] Lu-Dan Yu,[a] Nan Li,[a] Minhui Shen,[a] Xiaoru Peng,[a] Huangsheng Yang,[a] Yu-Xin Ye,[a] Fang Zhu,[a] Janusz Pawliszyn,[b] Jianqiao Xu *[a] and Gangfeng Ouyang *[acd]

Despite the excellent luminescent properties of lanthanide clusters (LnCs), their suprastructures that inherit their characteristic luminescent properties are scarcely reported. Herein, novel and highly luminescent suprastructures are synthesized *via* a two-step assembly method to incorporate LnCs in covalent organic frameworks (COFs). COFs are pre-synthesized and decorated with rigid anchoring groups on their nanochannel walls, which provide one-dimensional confined spaces for the subsequent *in situ* assembly of luminescent LnCs. The confined LnCs are termed nanoparticles (NPs) to distinguish them from the pure LnCs. Secondary micropores with predictable sizes are successfully formed between the walls of the nanochannels and the orderly aligned NPs therein. By using a small organic ligand that can efficiently sensitize Ln(III) cations in the assembly processes, the obtained composites show high quantum yields above 20%. The fluorescence can even be effectively maintained across nine pH units. The secondary micropores further enable the unambiguous discrimination of six methinehalides and ultrasensitive detection of uranyl ions. This study provides a new type of luminescent material that has potential for sensing and light emitting.

Introduction

The assembly of metal clusters (MCs) into ordered porous suprastructures has opened up a prominent avenue to efficient catalysis, separation, light emitting and sensing.[1–5] Nowadays, the adoption of MCs as the nodes of metal–organic frameworks (MOFs) has become the dominant route for constructing suprastructures of MCs, which enriches the structural diversities of MOFs and provides large numbers of accessible open metal sites therein.[1–4] Meanwhile, the engineered pores in these metal cluster frameworks are beneficial for promoting catalytic efficiencies and sensing selectivity through the confinement effects.[1,4] However, despite the excellent luminescent properties of lanthanide clusters (LnCs) that stem from their characteristic f–f transitions, *i.e.* sharp fluorescent emissions, large Stokes shifts, and long luminescence lifetimes,[6–9] the MOFs that incorporate highly luminescent LnCs remain scarcely reported.[10–12] Most of the reported luminescent MOFs that contain MC nodes emit light from their organic ligands based on the charge transfer between the precious metal clusters and the organic ligands.[3,4,13,14] The photoluminescence mechanisms are often very complicated and even distinct from each of such MOFs,[3,4,13,14] which imparts tremendous difficulty in rationally designing the suprastructure of LnCs with unambiguous photoluminescent properties.

On the other hand, although the highly efficient photoluminescence of LnCs has been clearly attributed to the antenna effects of organic ligands,[15–18] the synthesis of MOFs containing LnC nodes seems much more challenging than the synthesis of MOFs containing other MC nodes.[15–17] The popular one-pot bottom-up assembly methodology highly relies on the adoption of ligands with specific stereochemical characteristics to modulate the pore topologies,[15–17] owing to the intrinsically low coordination directionalities of the Ln(III) cations and the abundant coordination sites at the cluster nodes. Nowadays, the synthesis of MOFs with LnC nodes is still mainly based on empiricism and the trial-of-error strategy. Moreover, it also remains unclear whether the ligands can efficiently sensitize the LnCs or not. The sensitization of LnCs requires well-matched energy levels between the organic ligands and the Ln(III) cations. Luminescent MOFs that contain LnC nodes are frequently reported to emit fluorescence from their organic

[a]*MOE Key Laboratory of Bioinorganic and Synthetic Chemistry/KLGHEI of Environment and Energy Chemistry, School of Chemistry, Sun Yat-sen University, Guangzhou, Guangdong 510006, China. E-mail: xujq27@mail.sysu.edu.cn; cesoygf@mail.sysu.edu.cn*

[b]*Department of Chemistry, University of Waterloo, Waterloo, Ontario N2L3G1, Cananda*

[c]*Chemistry College, Center of Advanced Analysis and Gene Sequencing, Zhengzhou University, Kexue Avenue 100, Zhengzhou 450001, China*

[d]*Guangdong Provincial Key Laboratory of Emergency Test for Dangerous Chemicals, Guangdong Institute of Analysis (China National Analytical Center Guangzhou), Guangdong Academy of Sciences, 100 Xianlie Middle Road, Guangzhou 510070, China*

† Electronic supplementary information (ESI) available. See DOI: https://doi.org/10.1039/d2sc05915k

© 2022 The Author(s). Published by the Royal Society of Chemistry

Open Access Article. Published on 18 November 2022. Downloaded on 2/18/2026 2:20:38 PM. This article is licensed under a Creative Commons Attribution-NonCommercial 3.0 Unported Licence.

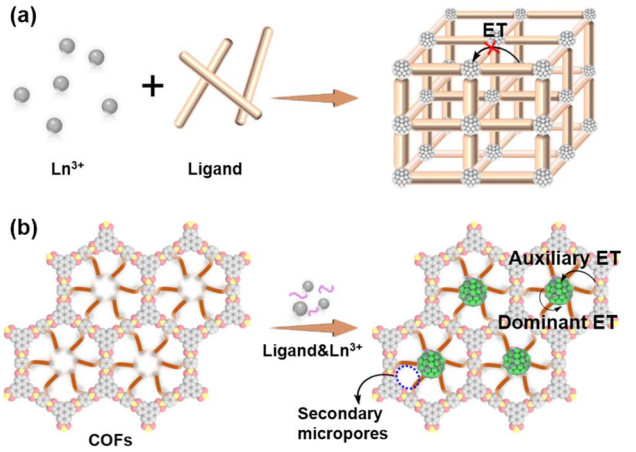

Scheme 1 Comparison between (a) the MOFs with LnCs as the nodes and (b) the current suprastructure synthesized by embedding LnCs in frameworks.

ligands.[10–12] The unmatched energy levels of those ligands might be attributed to the too large conjugation structures of the ligands, which results in too feeble excited states to donate energy to Ln(III) cations.[10] In other words, the construction of such MOFs that show the characteristic Ln(III) emissions requires dual-functional ligands for both modulating pore topologies and sensitizing Ln(III) cations.

Herein, inspired by the cutting-edge progress in embedding ultrafine nanoparticles in frameworks,[18–21] we propose a two-step assembly method for the facile preparation of novel and highly luminescent suprastructures. Covalent organic frameworks (COFs) are pre-synthesized and decorated with rigid anchoring groups on their nanochannel walls, which provide one-dimensional confined spaces for the subsequent *in situ* assembly of luminescent LnCs (Scheme 1). LnCs are directly observed to be orderly aligned in the one-dimensional nanochannels. Secondary micropores with predictable sizes are successfully formed between the walls of the nanochannels and the LnCs therein. Moreover, the current method allows the use of a small organic ligand that can efficiently sensitize Ln(III) cations in the assembly processes, which ensures the light emission from the LnCs. The obtained LnCFs show quantum yields above 20%. The secondary pores even enable the unambiguous discrimination of six methinehalides and ultrasensitive detection of uranyl ions. It is notable that the LnCs confined in the nanochannels are not likely to be uniform, which are different from the LnCs in the literature that possess homogeneous sizes and atomically precise structures.[6–9] Thus, they are termed ultrafine nanoparticles (NPs) below for clarity. And the novel suprastructures are termed lanthanide nanoparticle frameworks (LnNPFs).

Experimental results and discussion

Synthesis of COF1 and COF1-Heck

COF1 was synthesized *via* the imine condensation reaction by using 1,3,5-tri(4-aminophenyl)benzene (TAPB) and 2,5-divinylterephthalaldehyde (DVTPA) as the precursors (Fig. 1a, Text S1.3†). An AA stacking mode was present in COF1 (Fig. 1b), as confirmed by the X-ray diffraction (XRD) peaks at 2.75°, 4.80°, 5.60° and 7.50° that were corresponding to the 100, 110, 200 and 210 planes, respectively (Fig. 1c). The surface area of COF1 was determined to be 1851 $m^2 g^{-1}$ by the BET characterization (Fig. 1d). The pore size of COF1 was mainly focused on 23 Å, which also proved the AA stacking mode in COF1 (Fig. S1a†). Scanning electron microscopy (SEM) and transmission electron microscopy (TEM) further showed the nanofibrous morphology of COF1 (Fig. 1e and S2†). Fourier transform infrared (FTIR) spectra presented the characteristic band of C=N stretches around 1609 cm^{-1} in COF1, which resulted from the imine condensation reaction. Meanwhile, the bands of the N–H (3441 and 3360 cm^{-1}) and aldehydic C–H (2875 and 2775 cm^{-1}) stretches that belonged to the precursors disappeared, and the stretches of the vinyl groups in DVTPA shifted from 1050 cm^{-1} to 1065 cm^{-1} (Fig. S3†).

Rigid carboxyl groups were subsequently grafted to the vinyl bonds of COF1 as the anchoring sites of LnCs *via* the Heck reaction (termed COF1-Heck, Fig. 1a, Text S1.3†). COF1-Heck inherited the characteristic XRD patterns and the nanofibrous morphology of COF1 (Fig. 1c, f and S4†). The diameters of the carboxylated nanochannels were simulated to be 19 Å (Fig. 1b and S5†), which was consistent with the experimentally measured result (Fig. S1†). The BET surface area was reduced from 1851 to 731 $m^2 g^{-1}$ after the Heck reaction (Fig. 1d). Meanwhile, the IR absorption bands at 1645 cm^{-1} and 1300 cm^{-1} ascribed to the C=O and C–O stretches of the carboxyl groups, respectively, were observed (Fig. S6†). And as shown by the refined C 1s X-ray photoelectron spectra (XPS), the signal of carboxyl groups was also detected in COF1-Heck (Fig. S7†). The grafting yields were calculated to be 79.5% by the XPS data (Fig. S7†).

Assembly of TbNPs in COF1-Heck

In situ assembly of terbium nanoparticles (TbNPs) in COF1-Heck was performed through gradually evaporating the solvent to drive the precursors of TbNPs into the nanochannels (Text S1.4†). The BET surface area was dramatically decreased to 93 $m^2 g^{-1}$ after being embedded with TbNPs (Fig. S8†). Secondary micropores were characterized to be in the range from 8 to 16 Å (Fig. S8b and S8c†), consistent with the simulated results (Fig. S8d†). It was observed that Tb and Cl elements were uniformly distributed in the product (termed TbNPs@COF1-Heck) (Fig. 2a), although its morphology was almost indistinguishable to COF1-Heck according to the SEM and TEM characterization studies (Fig. S9†). Moreover, comparing the refined C 1s XPS spectrum of COF1-Heck and TbCs@COF1-Heck, the shifted signal of O–C=O verified the coordination of the carboxyl groups to Tb(III) in TbNPs@COF1-Heck (Fig. S7 and S10†).

Just as expected, TbNPs were highly aggregated and dominantly located outside of COF1, when the pristine COF1 was directly used as the substrate (Fig. S11†). Meanwhile, the pore size of this COF1-TbNP composite was slightly different from that of the pristine COF1, which demonstrated that the TbNPs

Open Access Article. Published on 18 November 2022. Downloaded on 2/18/2026 2:20:38 PM.
This article is licensed under a Creative Commons Attribution-NonCommercial 3.0 Unported Licence.

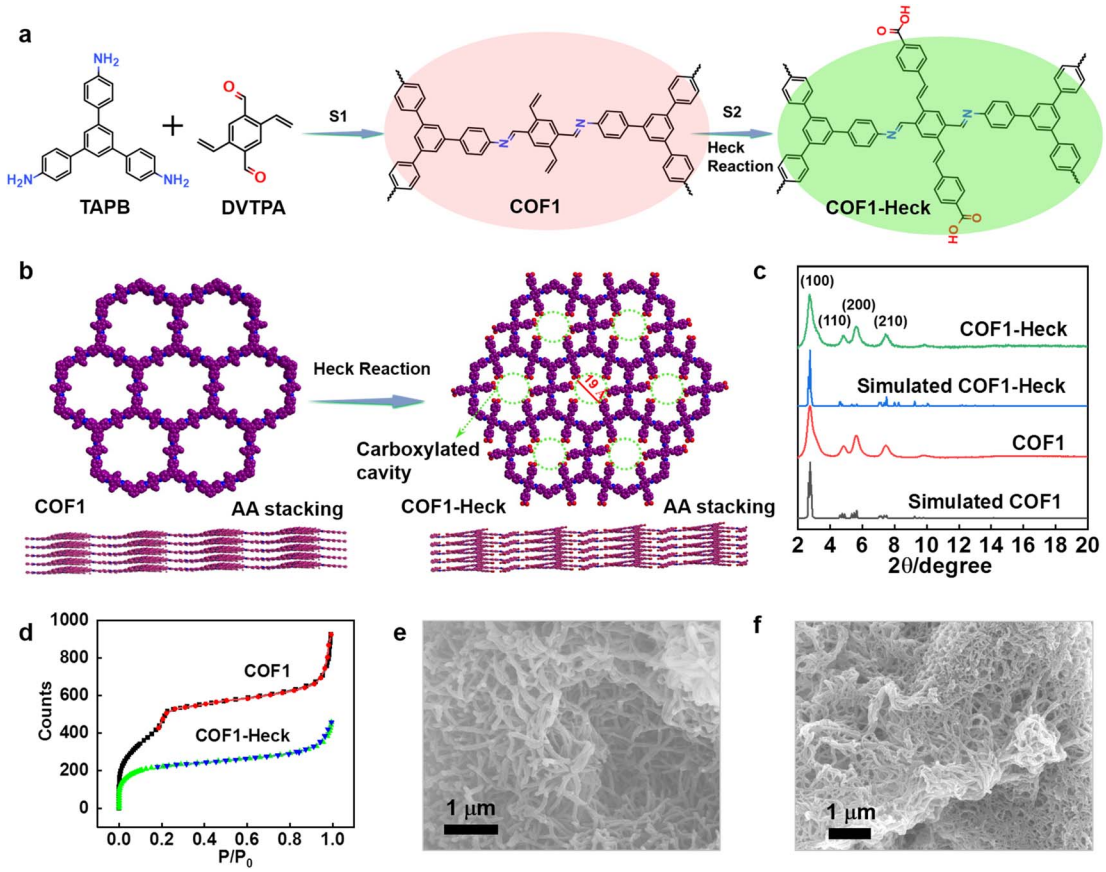

Fig. 1 (a) The overall steps for the preparation of COF1-Heck. (b) AA stacking modes of COF1 and COF1-Heck. The average diameter of the carboxylated nanochannels is about 19 Å. The C, N and O atoms are in purple, blue, and red, respectively. The H atoms are omitted for clarity. (c) Experimental and simulated XRD patterns of COF1 and COF1-Heck. (d) N_2 isothermal adsorption–desorption curves of COF1 and COF1-Heck. (e) SEM image of COF1. (f) SEM image of COF1-Heck.

were hardly embedded in the nanochannels of the pristine COF1 (Fig. S12†). Thus, it was inferred that the abundant carboxyl groups in COF1-Heck provided crucial seeding sites for the assembly of TbNPs. Subsequently, high-resolution high-angle annular dark field-scanning transmission electron microscopy (HAADF-STEM) was performed to characterize the embedded TbNPs. As shown in Fig. 2b, parallel strings of clusters were observed in TbNPs@COF1-Heck, while COF1-Heck was homogeneous in the view fields (Fig. S13†). These images clearly demonstrated that the TbNPs aligned orderly in the nanochannels. The size of the TbNPs in TbNPs@COF1-Heck was found to be about 19.4 Å by measuring the labelled area of TbNP@COF1-Heck (Fig. 2b and c), consistent with the average diameter of the carboxylated nanochannels (~19 Å, Fig. 1b and S5†). Thus, in combination with the secondary pores and the HAADF-STEM images, it could be concluded that TbNPs@COF1-Heck possesses the structure as shown in Scheme 1. Moreover, it is notable that the ultrafine nanoparticles were never observed in such an ordered manner in frameworks before.

For resolving the structure of the TbNPs in this new LnNPF, the XRD patterns of TbNPs@COF1-Heck were recorded. It was observed that the relative intensity of the peak at 5° in TbNPs@COF1-Heck was higher than that in COF1-Heck, which matched the highest peak of the pure TbCs that was synthesized in solution with the same precursors (Fig. S14 and S15,† in the following experiment, this kind of pure TbCs was used for comparison with the novel LnNPFs). It was inferred that the TbNPs in TbNPs@COF1-Heck and the pure TbCs synthesized in solution possessed similar crystalline structures. Then, the extended X-ray absorption fine structure (EXAFS) spectroscopy was used to further explore the coordination manners of the Tb cations in TbNPs@COF1-Heck (Fig. 2d–f, S16 and Table S1†). EXAFS fitting showed that the Tb–O or Tb–N interatomic distance was 2.37 ± 0.01 Å in TbNPs@COF1-Heck, which was consistent with the data from the single-crystal X-ray diffraction studies of the pure TbCs synthesized in solution (Table S1†). The nominal coordination number of Tb at a shell radius of 2.37 ± 0.01 Å in TbNPs@COF1-Heck was calculated to be 5.9 ± 0.5, which is also consistent with the pure TbCs (Table S1†). The similar interatomic distance and nominal coordination number also indicated that the TbNPs in TbNPs@COF1-Heck possessed a structure similar to the pure TbCs. Since water molecules and counter ions coordinated to the Tb(III) cations in the pure TbCs,[9] it was also inferred that water molecules and counter ions

© 2022 The Author(s). Published by the Royal Society of Chemistry

Open Access Article. Published on 18 November 2022. Downloaded on 2/18/2026 2:20:38 PM.
This article is licensed under a Creative Commons Attribution-NonCommercial 3.0 Unported Licence.

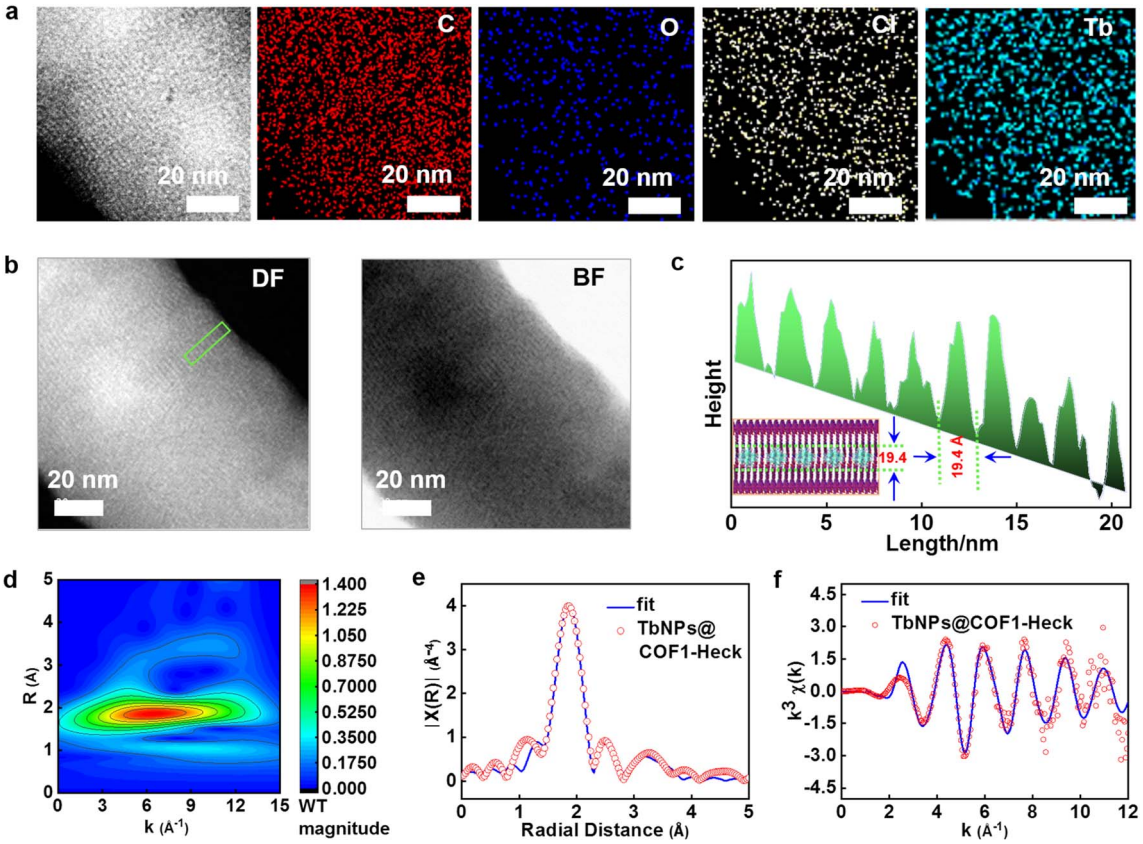

Fig. 2 (a) EDS mapping of the C, O, Cl and Tb elements in TbNPs@COF1-Heck. (b) HAADF images of TbNPs@COF1-Heck. DF represents the dark field. BF represents the bright field. (c) Size distribution of the TbNPs in COF1-Heck (derived from the highlighted part of TbNPs@COF1-Heck in (b)). Inset: diagram of the clusters in one of the nanochannels. (d) Tb K-edge EXAFS (points) and fit (line) for TbNPs@COF1-Heck, shown in k^3 weighted R-space. (e) Tb K-edge EXAFS (points) and fitted (line) oscillations of TbNPs@COF1-Heck, shown in k^3 weighted k-space. (f) Wavelet transform for the Tb k^3-weighted signal of TbNPs@COF1-Heck.

coordinated to the Tb(III) cations besides the organic ligands and the anchored carboxyl groups in TbNPs@COF1-Heck.

Tracking the assembly of TbNPs in COF1-Heck

For revealing the *in situ* assembly procedure of the TbNPs in COF1-Heck, the overall process was monitored at different time points (Fig. 3). After the 1st day, Tb was uniformly distributed in COF1-Heck while the chlorine atoms belonging to the small organic ligand (2-chloro-6-hydroxypyridine, CHP) were negligible in COF1-Heck (Fig. 3a). Besides, the IR absorption band at 1645 cm^{-1} ascribed to the carboxyl groups was shifted to 1638 cm^{-1} (Fig. 3d), which indicated the coordination of Tb^{3+} to the carboxyl groups on the nanochannel walls. The coordination of Tb^{3+} at the carboxyl sites probably provided a thermodynamic driving force that resulted in the more efficient diffusion of Tb^{3+} into the nanochannels than CHP. The anchoring of Tb^{3+} at the carboxyl sites could also subsequently cause the diffusion of the CHP molecules into the nanochannels.

The characteristic emission of Tb^{3+} on the 1st day was detected, although the intensity was quite weak (Fig. 3c and S17†). It was notable that the excitation peak of the composite was located at 290 nm on the 1st day, significantly different to the excitation peak of the pure TbCs that was located at 326 nm (Fig. 3b). It was indicated that COF1-Heck was capable of transferring energy to the carboxyl-anchored Tb^{3+} for triggering its emission on the 1st day. Prolonging the reaction time (1st to 5th day) gradually increased the emission intensity (Fig. 3c). The red shift of the excitation peak from 290 nm to 319 nm demonstrated that the energy donor was dominated by CHP at last (Fig. 3b). At the same time, the IR absorption band of the C–Cl stretches at 787 cm^{-1} gradually appeared (Fig. 3d). And as shown in Fig. 3f, the orderly aligned clusters become vivid along with increasing time, indicating that TbNPs had gradually formed in the nanochannels of COF1-Heck. However, on the 7th day, the emission of Tb^{3+} dramatically decreased in comparison with the 5th day (Fig. 3c), which was attributed to the severe aggregation of TbNPs outside COF1-Heck as observed in Fig. 3f. Besides, although the diffraction peak of the nanoclusters at 5.0° was overlapped with the 110 peak of COF1-Heck, it gradually becomes the highest peak in the composite in this tracing period, which further indicated that the TbNPs in TbNPs@COF1-Heck possessed a structure similar to the pure TbCs (Fig. 3e). According to the analysis above, the overall *in situ* assembly process of the TbNPs in COF1-Heck is illustrated in Fig. 3g.

© 2022 The Author(s). Published by the Royal Society of Chemistry

Open Access Article. Published on 18 November 2022. Downloaded on 2/18/2026 2:20:38 PM.
This article is licensed under a Creative Commons Attribution-NonCommercial 3.0 Unported Licence.

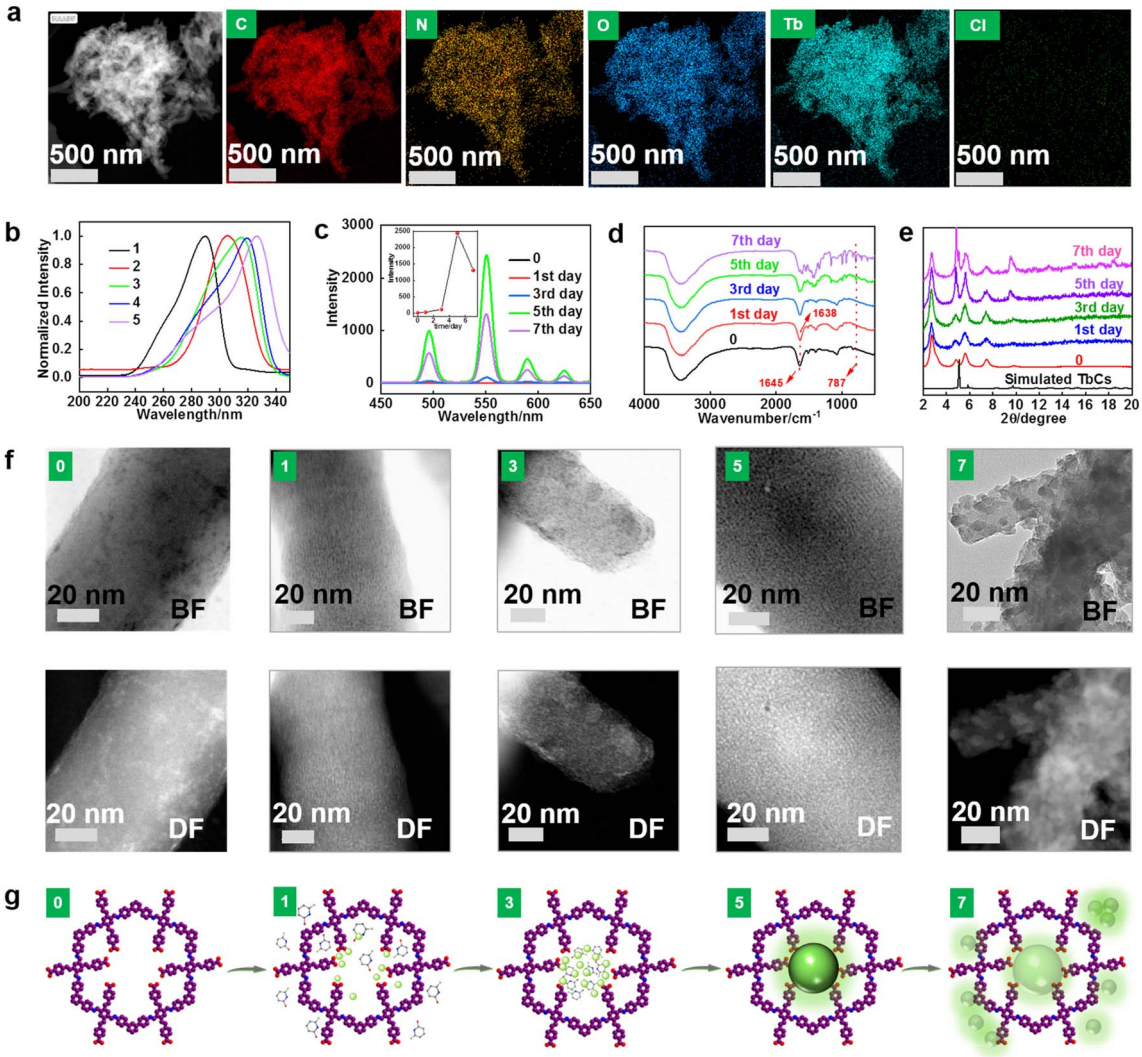

Fig. 3 (a) EDS mapping of the C, N, O, Tb and Cl elements on the 1st day. (b) Excitation spectra on the 1st day (curve 1), 3rd day (curve 2), 5th day (curve 3), and 7th day (curve 4). Excitation spectra of (curve 5) the pure TbCs. (c) Emission spectra from 0 to 7th day. Inset: fluorescence intensity at 550 nm from 0 to 7th day. (d) FTIR spectra from 0 to 7th day. (e) PXRD pattern from 0 to 7th day. (f) HAADF images from 0 to 7th day. (g) Schematic diagram of the TbNPs formed in COF1-Heck from 0 to 7th day.

The universality of the two-step assembly strategy

To explore the universality of this *in situ* assembly strategy, two other COFs with different pore sizes, termed COF2 and COF3 (Texts S1.6 and S1.7†), were chosen for investigation. The nanochannel diameters of COF2 and COF3 were measured to be 21 Å and 37 Å, respectively (Fig. S18†), which indicated the AA stacking modes in the two COFs. Consistent with COF1, the carboxyl anchoring sites for Tb^{3+} were introduced *via* the Heck reaction into COF2 and COF3. The obtained COF2-Heck and COF3-Heck were subsequently characterized (Fig. S19–S24†). The average diameters of the carboxylated nanochannels were simulated to be 13 Å for COF2-Heck and 27 Å for COF3-Heck, respectively (Fig. S25 and S26†).

Through following the aforementioned assembly strategy, clusters were also observed to be orderly aligned in the nanochannels of COF2-Heck (termed TbNPs@COF2-Heck). The average size of the TbNPs in COF2-Heck was measured to be 13.3 Å (Fig. S27†), which was close to the nanochannel diameter of COF2-Heck (13 Å). Secondary micropores were characterized to be in the range from 4 to 6 Å, consistent with the simulated results (Fig. S28†). By comparing with TbNPs@COF1-Heck, it could be concluded that the sizes of the TbNPs and the secondary pores were controllable *via* customizing the nanochannel dimensions of COFs. Besides, similar to COF1, the TbNPs were hardly embedded into the nanochannels when the pristine COF2 was not carboxylated (Fig. S29†).

In sharp contrast, when COF3-Heck was the substrate, no parallel strings of clusters were observed (Fig. S30†). Nonetheless, the characteristic XRD peaks of the pure TbCs were feasibly identified in this composite (also termed TbNPs@COF3-Heck for comparison with the other two composites, Fig. S31†). Meanwhile, it was observed that the pore size was nearly unchanged after the assembly of the TbNPs (Fig. S32†). It was speculated that the large pore size of COF3 leads to high

© 2022 The Author(s). Published by the Royal Society of Chemistry

Open Access Article. Published on 18 November 2022. Downloaded on 2/18/2026 2:20:38 PM. This article is licensed under a Creative Commons Attribution-NonCommercial 3.0 Unported Licence.

structural flexibility of COF3, which made it difficult to form a satisfying crystalline structure (Fig. S19†). The Heck reaction process was supposed to further ruin its one-dimensional nanochannels, thus limiting the formation of parallel clusters. Thus, it was concluded that the stable AA stacking modes of COFs were crucial for constructing ordered porous supra-structures of LnCs.

Characterization of the photoluminescent properties of TbNPs@COF-Heck

The excitation and emission spectra were similar among the composites (Fig. 3 and S33†). The photoluminescent quantum yields of the three TbNPs@COF-Heck composites were nearly equal to that of the pure TbCs, which were above 20% (Fig. 4a). In spite of the possible inner filtration effect (IFE) of COFs-Heck on the TbNPs (Fig. S34a†), the almost unchanged quantum yields of TbNPs@COF1-Heck and TbNPs@COF2-Heck should be partially attributed to the increased dispersity of the TbNPs that circumvented the aggregation-induced IFE present in the pure TbCs.

On the other hand, TbNPs@COF1-Heck and TbNPs@COF2-Heck showed shorter fluorescence lifetimes than the pure TbCs (Fig. S34b and Table S2†), which might be attributed to the additional sensitization pathway in the composites as described above. Meanwhile, non-irradiation decay was more likely to occur in these two composites than in the aggregated pure TbCs, due to the less restricted stretches of the surficial groups on the highly dispersed TbNPs and the possible presence of water molecules surrounding the highly dispersed TbNPs. The quantum yield and fluorescence lifetime of TbNPs@COF3-Heck were both nearly identical to those of the pure TbCs, which indicated that the dominant TbNPs were aggregated on the outer surfaces of COF3-Heck rather than embedding in the pores.

Furthermore, it was highly remarkable that TbNPs@COF1-Heck and TbNPs@COF2-Heck possessed much higher acid/base stabilities than the pure TbCs. No less than forty percent of the emission intensities were maintained in the pH range of 3 to 12 for TbNPs@COF1-Heck and TbNPs@COF2-Heck (Fig. 4b). In sharp contrast, the photoluminescence of TbNPs@COF3-Heck and the pure TbCs was quenched over eighty percent when the pH was lower than 4 or higher than 9. The promoted acid/base stability of TbNPs@COF1-Heck and TbNPs@COF2-Heck could be ascribed to the strong coordination bonds between the Tb(III) cations and the carboxyl groups in the nanochannels, as well as the structural rigidity resulting from confinement of the nanochannels. The high acid/base stabilities also indicated that TbNPs in COF1-Heck and COF2-Heck could be protected from erosion by water and other complexing reagents. Thus, TbNPs@COF1-Heck and TbNPs@COF2-Heck are useable as photoluminescent probes even in complicated sample matrices.

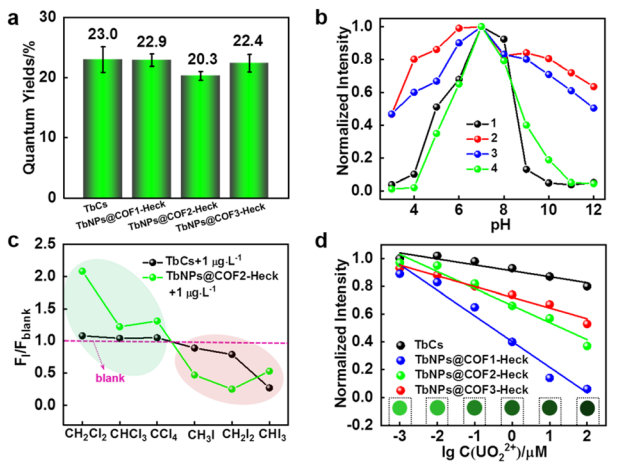

Fig. 4 (a) Photoluminescent quantum yield of the pure TbCs, TbNPs@COF2-Heck, TbNPs@COF1-Heck, and TbNPs@COF3-Heck, respectively. The error bars represent the standard deviations ($n = 3$). (b) Normalized fluorescence intensities of the pure TbCs (curve 1), TbNPs@COF1-Heck (curve 2), TbNPs@COF2-Heck (curve 3) and TbNPs@COF3-Heck (curve 4) at pH from 3–12, respectively. (c) Fluorescent response of the pure TbCs and TbNPs@COF2-Heck after addition of 1 μg L^{-1} of CH_2Cl_2, $CHCl_3$, CCl_4, CH_3I, CH_2I_2 and CHI_3 in methanol, respectively. The fluorescence intensities at 545 nm were measured for investigation. (d) Fluorescent response of the pure TbCs, TbNPs@COF1-Heck, TbNPs@COF2-Heck and TbNPs@COF3-Heck to UO_2^{2+}, respectively. Inset: Photos of TbNPs@COF1-Heck suspensions after treatment with different contents of UO_2^{2+} (0.001–100 μM) under the excitation of a handhold 310 nm UV light source.

Discrimination of methinehalide

The obtained TbNPs@COF2-Heck was used to discriminate methinehalides, as the sizes of the secondary micropores were supposed to exhibit steric effects for the entry of methinehalides (Fig. S28 and S35†). Methinehalides are extensively used solvents and chemical raw materials. They are suspected to cause chronic toxicity, mutagenicity, and carcinogenicity.[22,23] The presence of CH_2Cl_2 triggered the most significant fluorescence increase of TbNPs@COF2-Heck, followed by CCl_4. $CHCl_3$ triggered the least emission increase (Fig. 4c and S36†). In comparison, the fluorescence of TbNPs@COF2-Heck was dramatically quenched by CH_3I, CH_2I_2 and CHI_3. The response intensities were well consistent with the minimum limit sizes of these molecules (Fig. S35†). In sharp contrast, the pure TbCs showed negligible fluorescent responses to these molecules except for CHI_3 (Fig. S37†).

It was supposed that the smaller CH_2Cl_2 and CCl_4 molecules could enter the secondary pores of TbNPs@COF2-Heck more feasibly than $CHCl_3$, and suppress the stretches of the surficial OH groups and water molecule inside the nanochannels through steric effects, thus leading to significant enhancement of photoluminescence. An evidence was unambiguously given by the increased photoluminescence lifetime of TbNPs@COF2-Heck from 1.54 ms to 2.01 ms after 30 μg L^{-1} CH_2Cl_2 was added. In comparison, the fluorescence lifetime of the pure TbCs was only changed from 1.86 ms to 1.89 ms under the same conditions (Fig. S38 and Table S2†). Moreover, IFE was judged to be the quenching mechanism of CH_2I_2 and CHI_3 owing to their absorption spectra being highly overlapped with the excitation spectrum of the composite (Fig. S39†). CHI_3 showed less significant absorption in the same region, and could only be present outside the micropores to cause the IFE effect owing to its larger molecular size. All in all, the discrimination of six

Open Access Article. Published on 18 November 2022. Downloaded on 2/18/2026 2:20:38 PM. This article is licensed under a Creative Commons Attribution-NonCommercial 3.0 Unported Licence.

methinehalides was achieved by using TbNPs@COF2-Heck, which was difficult to realize with the pure TbCs or other conventional fluorescent probes.

Ultrasensitive sensing of the hazardous ion, UO_2^{2+}

Furthermore, the sensing performances of the pure TbCs and the TbNPs@COF-Heck composites were investigated for the detection of uranyl ions (UO_2^{2+}). UO_2^{2+} exhibits high chemotoxicity, which can lead to irreversible kidney damage and urinary system diseases.[24,25] As shown by the slopes of the curves in Fig. 4d, TbNPs@COF1-Heck exhibited the highest sensitivity, followed by TbNPs@COF2-Heck. TbNPs@COF3-Heck showed a sensitivity equivalent to that of the pure TbCs. The higher sensitivity should be attributed to the high microporosity that increased the accessible surface areas of the TbNPs. Quantitative detection of UO_2^{2+} was achieved in the concentration range from 0.001 to 100 μM (Fig. 4d). The limit of detection (LOD) of TbNPs@COF1-Heck for UO_2^{2+} was low to 0.38 nM, nearly three orders of magnitude below the restriction limit in drinking water (130 nM) set by the United States Environmental Protection Agency (USEPA), and two orders of magnitude lower than the pure TbCs (35 nM). The sensitivity achieved by using TbNPs@COF1-Heck was even superior to many other reported optical methods (Table S3†).

Conclusions

In this study, new luminescent LnNPFs are synthesized *via* a two-step assembly method. Similar to the previous MOFs containing LnC nodes that are synthesized from the one-pot bottom-up assembly method, the current LnNPFs also possess ordered and designable structures. The sizes of the LnNPs and the secondary pores in the new suprastructures are proven tunable by using COFs of different nanochannel dimensions. It is even possible to tune the sizes of the secondary pores by using rigid anchoring groups of different sizes in the future. More importantly, the characteristic luminescent properties of Ln(III) are present in the new LnNPFs. It was highly challenging to incorporate these luminescent properties in the previous MOFs, as dual-functional organic ligands were required for both modulating pore topologies and sensitizing Ln(III) cations. The present method is convenient and effective by preliminarily constructing frameworks and subsequently assembling luminescent LnNPs in the nanochannels of the frameworks in two steps. The high photoluminescent quantum yields and stabilities, and the successful applications in discriminating methinehalides and detecting UO_2^{2+}, unambiguously demonstrate that the new luminescent LnNPFs have high potential for light emitting and sensing in the future.

Data availability

The authors declare that the data supporting the findings of this study are available within the paper and the ESI,† as well as from the authors upon request.

Author contributions

Y.-J. Tong prepared the materials, studied the fluorescent properties and wrote the manuscript; L.-D. Yu, N. Li, M. Shen, X. Peng, H. Yang and Y.-X. Ye helped with the characterization studies of BET, SEM, TEM, FTIR, XPS, and EXAFS and structural simulations; J. Xu designed the experiment and helped with the funding acquisition and supervision. F. Zhu, J. Pawliszyn and G. Ouyang helped with project administration, review and editing.

Conflicts of interest

There are no conflicts to declare.

Acknowledgements

Thankful for the support of the Key-Area Research and Development Program of Guangdong Province (2020B1111350002), the National Key Research and Development Program of China (2017YFE0133200), the National Natural Science Foundation of China (22122612, 22036003, 21806188 and 22076222), the NSF of Guangdong Province (2018A030313324), Guangzhou Science and Technology Planning Project (202102020329 and 201803030018), and the Fundamental Research Funds for the Central Universities (2021qntd24).

Notes and references

1 L. Feng, J. Pang, P. She, J.-L. Li, J.-S. Qin, D.-Y. Du and H.-C. Zhou, *Adv. Mater.*, 2020, **32**, 2004414.
2 L. Yu, S. Ullah, K. Zhou, Q. Xia, H. Wang, S. Tu, J. Huang, H.-L. Xia, X.-Y. Liu, T. Thonhauser and J. Li, *J. Am. Chem. Soc.*, 2022, **144**, 3766–3770.
3 Z. Wei, Z.-Y. Gu, R. K. Arvapally, Y.-P. Chen, R. N. McDougald, J. Ivy, A. Yakovenko, D. Feng, M. Omary and H.-C. Zhou, *J. Am. Chem. Soc.*, 2014, **136**, 8269–8276.
4 R.-W. Huang, Y.-S. Wei, X.-Y. Dong, X.-H. Wu, C.-X. Du, S.-Q. Zang and T. Mak, *Nat. Chem.*, 2017, **9**, 689–697.
5 I. Colliard and M. Nyman, *Angew. Chem., Int. Ed.*, 2021, **60**, 7308–7315.
6 M.-H. Du, L.-Q. Chen, L.-P. Jiang, W.-D. Liu, L.-S. Long, L. Zheng and X.-J. Kong, *J. Am. Chem. Soc.*, 2022, **144**, 5653–5660.
7 D. Thielemann, A. Wagner, E. Rösch, D. Kölmel, J. Heck, B. Rudat, M. Neumaier, C. Feldmann, U. Schepers, S. Bräse and P. Roesky, *J. Am. Chem. Soc.*, 2013, **135**, 7454–7457.
8 D. Gálico and M. Murugesu, *Angew. Chem., Int. Ed.*, 2022, **61**, e202204839.
9 D. Gálico, A. Kitos, J. Ovens, F. Sigoli and M. Murugesu, *Angew. Chem., Int. Ed.*, 2021, **60**, 6130–6136.
10 Z. Ajoyan, G. Mandl, P. Donnarumma, V. Quezada-Novoa, H. Bicalho, H. Titi, J. Capobianco and A. Howarth, *ACS Mater. Lett.*, 2022, **4**, 1025–1031.
11 D. Gallis, D. Vogel, G. Vincent, J. Rimsza and T. Nenoff, *ACS Appl. Mater. Interfaces*, 2019, **11**, 43270–43277.

© 2022 The Author(s). Published by the Royal Society of Chemistry

Open Access Article. Published on 18 November 2022. Downloaded on 2/18/2026 2:20:38 PM.
This article is licensed under a Creative Commons Attribution-NonCommercial 3.0 Unported Licence.

12 Y. Zhang, L. Huang, H. Miao, H. Wan, H. Mei, Y. Liu and Y. Xu, *Chem.–Eur. J.*, 2015, **21**, 3234–3241.
13 J. Perego, C. Bezuidenhout, I. Villa, F. Cova, R. Crapanzano, I. Frank, F. Pagano, N. Kratochwill, E. Auffray, S. Bracco, A. Vedda, C. Dujardin, P. Sozzani, F. Meinardi, A. Comotti and A. Monguzzi, *Nat. Commun.*, 2022, **13**, 3504.
14 X.-Y. Dong, Y. Si, J.-S. Yang, C. Zhang, Z. Han, P. Luo, Z.-Y. Wang, S.-Q. Zang and T. Mak, *Nat. Commun.*, 2020, **11**, 3678.
15 X.-L. Lv, L. Feng, L.-H. Xie, T. He, W. Wu, K.-Y. Wang, G. Si, B. Wang, J.-R. Li and H.-C. Zhou, *J. Am. Chem. Soc.*, 2021, **143**, 2784–2791.
16 Y. Feng, X. Xin, Y. Zhang, B. Guo, F. Li, X. Kong, Y. Wang, X. Wang, Y. Wang, L. Zhang and D. Sun, *Cryst. Growth Des.*, 2019, **19**, 1509–1513.
17 Z. Chen, Ł. Weseliński, K. Adil, Y. Belmabkhout, A. Shkurenko, H. Jiang, P. Bhatt, V. Guillern, E. Dauzon, D.-X. Xue, M. O'Keefe and M. Eddaoudi, *J. Am. Chem. Soc.*, 2017, **139**, 3265–3274.
18 Z. Jiang, X. Xu, Y. Ma, H. S. Cho, D. Ding, C. Wang, J. Wu, P. Oleynikov, M. Jia, J. Cheng, Y. Zhou, O. Terasaki, T. Peng, L. Zan and H. Deng, *Nature*, 2020, **586**, 549–554.
19 G. Li, S. Zhao, Y. Zhang and Z. Tang, *Adv. Mater.*, 2018, **30**, 1800702.
20 Q. Yang, Q. Xu and H. Jiang, *Chem. Soc. Rev.*, 2017, **46**, 4774–4808.
21 M. Lu, M. Zhang, J. Liu, T. Yu, J. Chang, L. Shang, S. Li and Y. Lan, *J. Am. Chem. Soc.*, 2022, **144**, 1861–1871.
22 F. Lin, L. Xiang, Z. Zhang, N. Li, B. Yan, C. He, Z. Hao and G. Chen, *Crit. Rev. Environ. Sci. Technol.*, 2022, **5**, 311–355.
23 A. Artabe, H. Cunha-Silva and A. Barranco, *Food Chem. Toxicol.*, 2020, **145**, 111677.
24 Y.-J. Tong, L.-D. Yu, Y. Huang, Q. Fu, N. Li, S. Peng, S. Ouyang, Y.-X. Ye, J. Xu, F. Zhu, J. Pawliszyn and G. Ouyang, *Anal. Chem.*, 2021, **93**, 9226–9234.
25 J. Lee, Z. Wang, J. Liu and Y. Lu, *J. Am. Chem. Soc.*, 2008, **130**, 14217–15142.